



## Radio Science

### RESEARCH ARTICLE

10.1002/2015RS005841

This article is a companion to Carrano and Rino [2016] doi:10.1002/2015RS005903.

#### Special Section:

Ionospheric Effects Symposium 2015

#### Key Points:

- Power law classification of four years C/NOFS parallel Langmuir probe data
- Identification of recurrent power law structure change
- Association of two-component power law with most highly disturbed data segments

#### Correspondence to:

C. L. Rino,  
crino@comcast.net

#### Citation:

Rino, C. L., C. S. Carrano, K. M. Groves, and P. A. Roddy (2016), A characterization of intermediate-scale spread  $F$  structure from four years of high-resolution C/NOFS satellite data, *Radio Sci.*, 51, 779–788, doi:10.1002/2015RS005841.

Received 22 OCT 2015

Accepted 8 APR 2016

Accepted article online 2 MAY 2016

Published online 27 JUN 2016

## A characterization of intermediate-scale spread $F$ structure from four years of high-resolution C/NOFS satellite data

Charles L. Rino<sup>1</sup>, Charles S. Carrano<sup>1</sup>, Keith M. Groves<sup>1</sup>, and Patrick A. Roddy<sup>2</sup>

<sup>1</sup>Institute for Scientific Research, Boston College, Boston, Massachusetts, USA, <sup>2</sup>Air Force Research Laboratory, Kirtland AFB, Albuquerque, New Mexico, USA

**Abstract** Power law spectra have been invoked to interpret equatorial scintillation data for decades. Published analyses of intensity and phase scintillation data typically report power law spectra of the form  $q^{-p}$  with  $2.4 < p < 2.6$ . However, in situ rocket and satellite measurements of equatorial spread  $F$  have shown evidence of spectra with two power law components. Strong scatter simulations and recent theoretical results have shown that two-component power law spectra can reconcile simultaneous equatorial scintillation observations from VHF to S-Band. The Communication/Navigation Outage Forecasting System (C/NOFS) satellite Planar Langmuir Probe generated a multiyear high-resolution sampling of equatorial spread  $F$ , but published analyses to date have reported only single-component power laws over scales from tens of kilometers to 70 m. This paper summarizes the analysis of high-resolution C/NOFS data collected over the four year period 2011 to 2014. Following an earlier investigation of several months of C/NOFS data by the authors of this paper, the extended data set revealed a pattern of occurrence of two-component spectra in the most highly disturbed data sets. The results confirm a known inverse correlation between turbulent strength and spectral index. The new results are interpreted as an equatorial spread  $F$  life cycle pattern with two-component spectra in the early development phase giving way to single-component spectra in the decay phase.

### 1. Introduction

The phenomena collectively referred to as equatorial spread  $F$  (ESF) evolve from a broad range of scale-dependent ionospheric processes. For this study ionospheric structure is divided into large-scale, intermediate-scale, and small-scale regimes. The large-scale regime includes the background ionosphere and the quasi-equilibrium processes that sustain it. The intermediate-scale regime includes the prominent ESF depletions and associated structure. The small-scale regime includes structure in the diffusion range, which supports the radar backscatter that delineates plumes. Partitioning ionospheric processes by scale constrains both spatial and temporal variations. The intermediate-scale regime, which is the subject of this study, is temporally invariant over typical measurement intervals, whereby data acquired by in situ probes can be interpreted as one-dimensional scans through a *frozen* structure.

A wavelet-based analysis procedure was developed for processing high-resolution data from the Planar Langmuir Probe (PLP) instrument aboard the Air Force Communication/Navigation Outage Forecasting System (C/NOFS) satellite Rino *et al.* [2014]. To review the essential elements of the procedure, high-resolution PLP data from each C/NOFS pass are resampled to a uniform spatial grid. The resampled data subtend upward of 20,000 km with 10 m sampling. Discrete wavelet transforms (DWTs) generate 17 logarithmic scales. At each scale there are  $N_j = 2^{J-j}$  DWT samples where  $j$  is the scale index,  $J = \log_2(N)$ , and  $N$  is the next power of 2. It was found by inspection of the DWT variations at each scale that scales larger than  $j = 12$  were not resolved sufficiently for statistical averaging. The wavelet at  $j = 12$  has a support of 260 km, which defines the largest segment length within the data span that can be reliably characterized by a spectral density function (SDF).

Scale spectra are computed by averaging over the segment DWT intensity samples at each of the 12 logarithmic scales. Scale spectra are saved in dB units along with the base 10 logarithm of the wave numbers corresponding to the spatial scales. The following one-dimensional SDF is hypothesized to characterize the

structure from the smallest resolved wave number,  $\Delta q = 2\pi/L_s$  where  $L_s$  is the segment length, to the largest wave number,  $\pi/\Delta s$  where  $\Delta s$  is the spatial resolution:

$$\varphi(q) = \begin{cases} C_1 q^{-p_1} & q < q_0 \\ C_2 q^{-p_2} & q > q_0 \end{cases} \quad (1)$$

Continuity at the break wave number  $q_0$  imposes the constraining relation

$$C_2 = C_1 q_0^{p_2 - p_1} \quad (2)$$

Hereafter the index  $p$  will refer to one-dimensional in situ structure. Positive  $p$  implies an inverse power law.

To test the two-component hypothesis, the 12 scale spectra samples are partitioned into two-component sets  $[1 : np]$  and  $[np + 1 : 12]$  where  $3 \leq np \leq 10$ . A linear least squares (lls) fit applied to each set generates  $C$  and  $p$  estimates. An overall lls fit is calculated for each partition. The partition with the smallest overall lls error is selected, whereby every segment is characterized by the parameters  $C_1, p_1, C_2, p_2, np$ , and the lls goodness of fit.

The first classification operation selects a minimum lls threshold that partitions the segments into unstructured and structured classes. Determining an appropriate threshold is a judgment guided by simulations and the C/NOFS data. In our earlier study, the smaller number of data segments led us to a stringent acceptance threshold [Rino *et al.*, 2014]. We were seeking classification with the fidelity shown in Rino *et al.* [2014, Figure 13]. In light of the much larger four year data set, we found this criterion to be much too restrictive.

To complete the classification, structured segments with  $p_1 \approx p_2$  are classified as a single component. Structured two-component segments with  $p_2 \approx 0$  are classified as noise limited. Structured segments with  $p_1 < p_2$  are classified as two components. For two-component spectra a break wave number is estimated from the relation

$$q_0 = (C_2/C_1)^{1/(p_2 - p_1)}, \quad (3)$$

which is formally an interpolation between the two wave numbers that delineate the large-scale and small-scale components.

Before presenting the new results, the next section summarizes published C/NOFS structure studies. The summary includes multi-instrument measurements, plume-occurrence statistics, in situ structure/scintillation correlations, and structure simulations.

## 2. A Survey of C/NOFS Structure Studies

Nishioka *et al.* [2008] modified the SAMI2 ionospheric model to reconcile predicted large-scale structure with data from two evening C/NOFS passes recorded during a solar activity quiet period in October 2008. Data from the Jicamarca radar identified coincident plumes. Enhanced UHF/VHF scintillation was observed on paths that intercepted the highest-density regions but not necessarily from the most highly structured C/NOFS passes. A single power law with  $1.5 < p < 1.8$  characterized the C/NOFS spectra to the wavelength corresponding to 70 m where the spectra transitioned to a much steeper index. The largest reported 250 MHz scintillation index was 0.8. Rodrigues *et al.* [2009] compared high-resolution density structures and  $E$  field structures with emphasis on the diffusion regime. Spectral characteristics reported by Rodrigues *et al.* [2009] were identical to those reported by Nishioka *et al.* [2008].

Studies by Huang *et al.* [2011], Klenzing *et al.* [2011], Aveiro *et al.* [2012], Huang *et al.* [2013, 2014], and Costa *et al.* [2014] address the taxonomy and occurrence properties of plumes. A study by Dao *et al.* [2012] addresses plume electron density variation along magnetic field lines.

The plume generation mechanism is attributed to a convective instability that generates a turbulence-like cascade of structure from the largest initiating scales to scales in the diffusion range where the structure is dissipated. Plume taxonomy remains an active area of research, but few attempts have been made to characterize the stochastic intermediate-scale structure since Hysell's survey paper [Hysell, 2000]. Current intermediate-scale simulations, e.g. Aveiro *et al.* [2012], do not resolve structure smaller than 10 km. A more recent paper by Retterer and Roddy [2014] discussed the morphology of ESF and the role of bottomside perturbation seeds. Figure 4 in that study shows an SDF with an index near 2 from 1 km to 60 m.

An important C/NOFS objective is predicting and extrapolating (nowcasting) outages caused by scintillation [de La Beaujardiere, 2003]. The effort has been hampered by the lack of a viable strong scatter theory, but weak-scatter theory has been used extensively to reconcile intermediate-scale structure measured by C/NOFS with scintillation observations. Roddy *et al.* [2010] verified the correlation between enhanced C/NOFS intermediate-scale structure and coincident UHF scintillation observed at the Christmas Island station of the SCINDA network.

Costa *et al.* [2011] performed a detailed study using a three-dimensional model with a product of cross-field and field-aligned SDF components. The intermediate-scale transverse structure was modeled by the single intermediate-scale power law. Figure 4 in that study summarizes scintillation intensity spectra with an overlay of the C/NOFS single intermediate-scale power law model. Costa *et al.* [2011] also developed an analysis procedure to associate path-integrated structure with the model calculations. Good model-structure agreement was achieved for weak to moderate UHF scintillation. A wavelet-based analysis was published by Stoneback *et al.* [2013], who exploited the spatial-filtering properties of continuous wavelet transformations to extract variance measures. The variance measures were used to scale an hypothesized single power law SDF. Results reported by Stoneback *et al.* [2013] were comparable to the results reported by Costa *et al.* [2011].

From the published C/NOFS intermediate-scale structure studies and other active ESF research, the underlying mechanism is well in hand. Moreover, strong UHF scintillation can be reconciled with a single-component power law with an in situ power law index less than 2 [Franke *et al.*, 1984]. There is a break in the diffusion scale range (70 to 80 m) where the spectrum steepens. Theoretical support for the single power law is provided by “inverted V” structures observed in rocket data by Hysell [2000].

### 3. C/NOFS ESF Structure Summary

The unclassified segment scale spectra provide periodogram-like maps of ESF activity. For example, Figure 1 shows the altitude dependence of the scale spectra dB intensity levels at the wavelet scales closest to 10 km and 1 km. On average, the larger-scale intensity exceeds the smaller-scale intensity and both measures decrease with increasing altitude. The high degree of variability is intrinsic to ESF. Realizations constructed by inverse Fourier transformation of uncorrelated samples with an imposed inverse power law have much less variability. The average variation with altitude follows the average altitude variation of the segment mean electron density. It is a common practice to normalize spectral estimates to a measure of the background electron density. Absolute measures are used in this study to facilitate application of the results to predicting satellite propagation disturbances.

We note in passing that the 2014 monotonic decrease with increasing altitude is disrupted about 450 km. Although the height of the F layer cannot be ascertained directly from C/NOFS data, the 2014 structure

variation can be explained by C/NOFS sampling lower density structure below the F region peak. Insofar as the ESF structure is concerned, the turbulent structure levels track mean electron density levels.

The 10 km structure intensity shown in Figure 1 varies from less than 50 dB to more than 100 dB. Strong ESF activity, e.g., the occurrence of plumes, should be associated with the largest structure levels. To support this conjecture, Figure 2 shows the local time occurrence of 10 km scale spectra intensity levels greater than 100 dB. For uniformity, only the segments below 600 km were included in the summaries. The peak occurrence of enhanced 10 km structure occurs approximately 4 h before local midnight. The result is

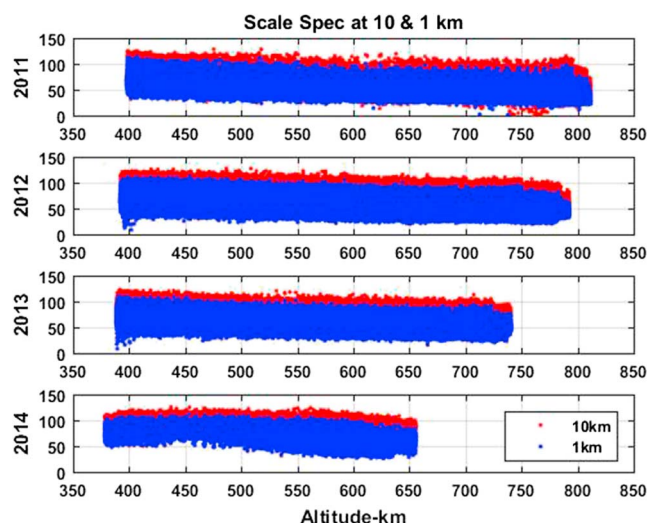


**Figure 1.** Yearly scale-spectrum dB intensity at 10 and 1 km scales versus C/NOFS altitude.

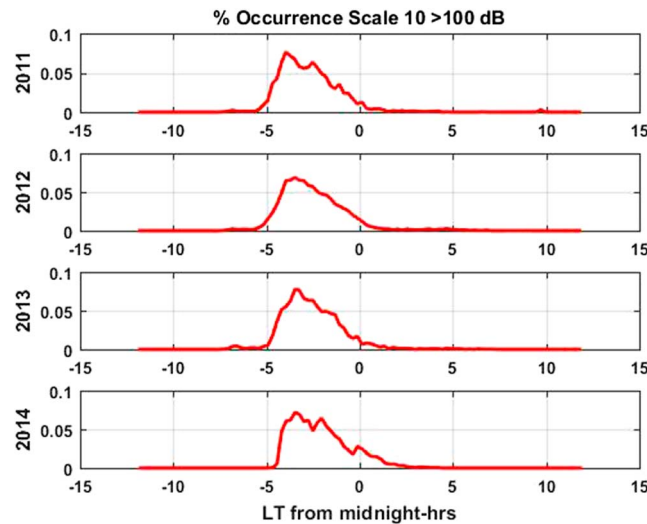


**Figure 2.** Local time occurrence of 10 km scale spectrum intensity >100 dB.

PLP noise floor, although a transition to a steeper slope could be obscured by PLP noise. However, we shall see that the two-component class of primary interest is associated with the most highly disturbed (least affected by PLP noise) segments. Thus, incorrectly classified single-component segments are likely to be confined to spectra with transitions in the small-scale regime. The small-scale regime is more accurately measured with the smaller 10 km segments used in the summarized C/NOFS studies.

Figures 3–6 summarize the structured segment characteristics by year. Figures 3–6 (left) are a  $C_1$  versus  $p_1$  scatter diagram. The single-component contributions are shown in blue. The two-component contributions are shown in red. The fraction in the title in Figures 3–6 (left) is the number of structured segments over the total number of segments. Figures 3–6 (right) summarize the two-component segments. Figures 3–6 (top right) shows the  $p_1$  (magenta) and  $p_2$  (green) estimates versus altitude. Figures 3–6 (bottom) show the base

consistent with reported manifestations of ESF activity in the summary section. The association of enhanced intermediate-scale structure with plume development and taxonomy is beyond the scope of the current study, but the occurrence patterns provide an important starting point for such studies.

The structured segments are classified as single power law noise-limited, single power law, and two-component power law. The single-component noise-limited spectra are two-component spectra with  $p_2 \approx 0$ , which is the largest class of structure segments. As in our initial study, the class of single-component power law segments is combined with the noise-limited class [see Rino *et al.*, 2014, Figure 8]. Estimates of  $C_1$  and  $p_1$  are unaffected by the

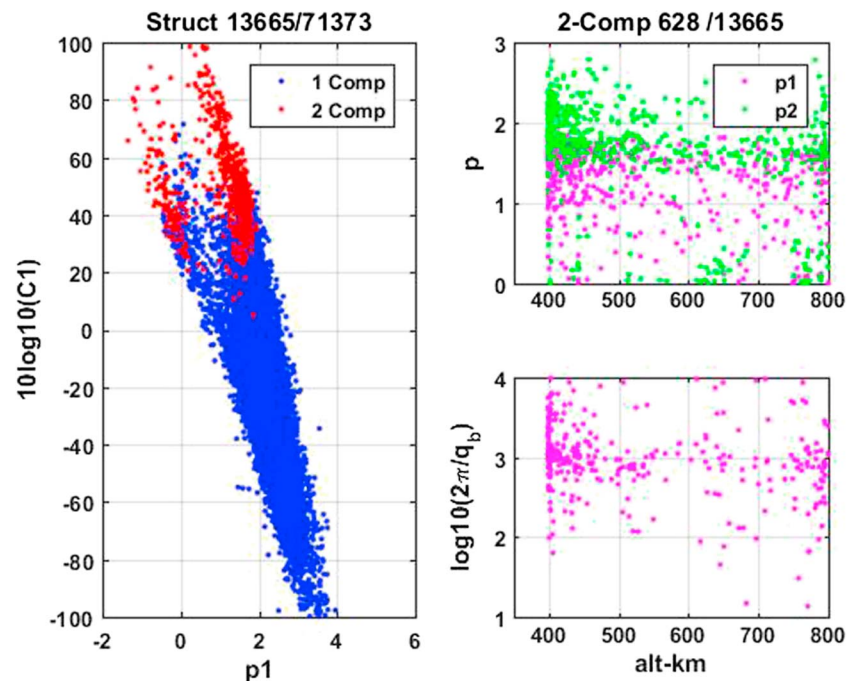


**Figure 3.** Summary of structured scale spectra for 2011 segments. (left) A scatter diagram of  $p_1$  versus  $C_1$ . (top right) Two-component indices versus altitude. (bottom right) Break scale versus altitude.

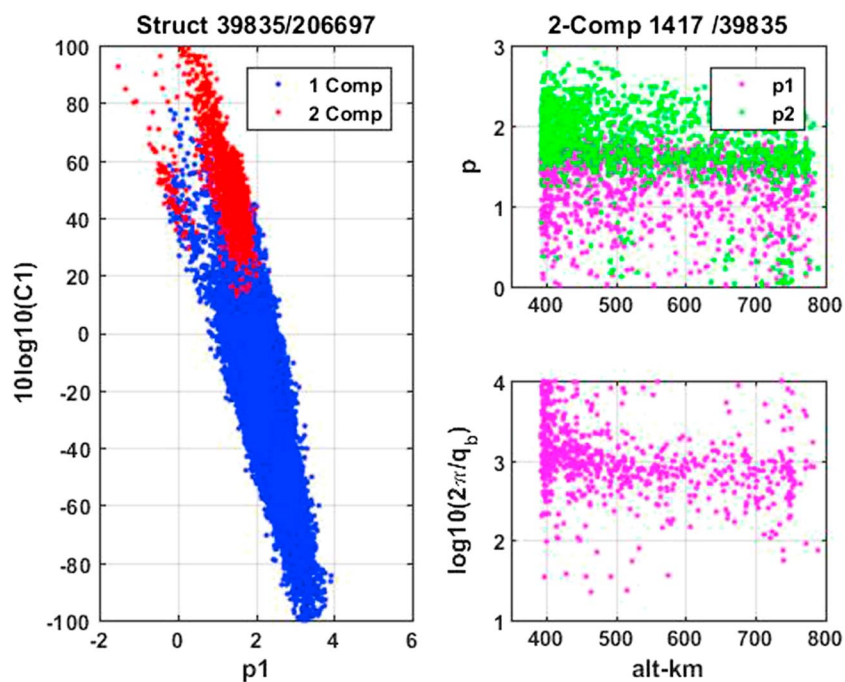


Figure 4. Summary of structured scale spectra for 2012 segments.

10 logarithm of estimated break scale versus altitude. The fraction in the title in Figures 3–6 (right) is the ratio of the number of two-component spectra divided by the repeated number of structured spectra.

To illustrate the classification threshold sensitivity, Figure 7 shows the summary of the 2011 data reprocessed at the threshold that was used in the initial study. Upon comparing Figure 7 with Figure 3, one can see the better definition of the two-component structure. The lower acceptance threshold enhanced the structured segment class by an order of magnitude.

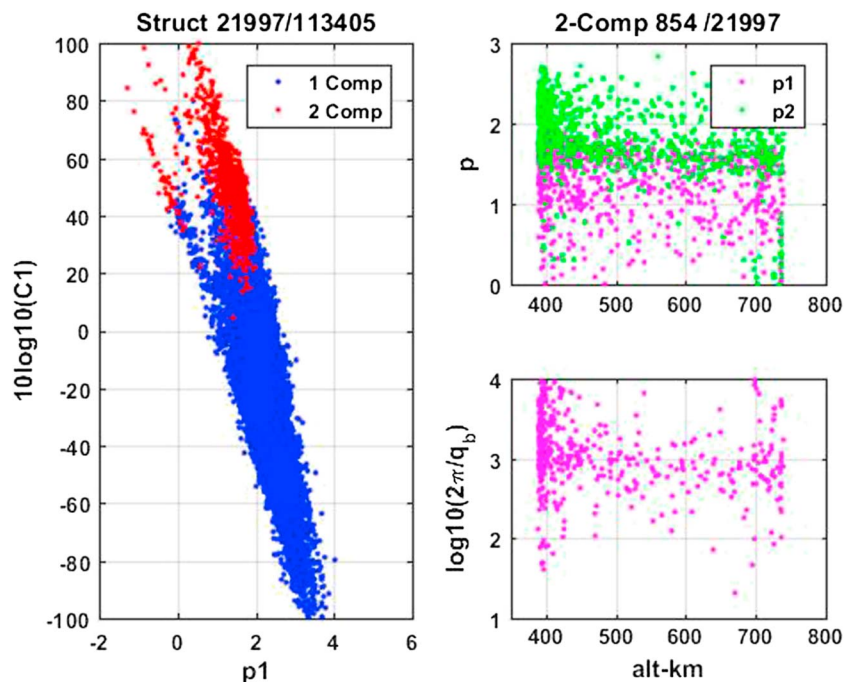


Figure 5. Summary of structured scale spectra for 2013 segments.

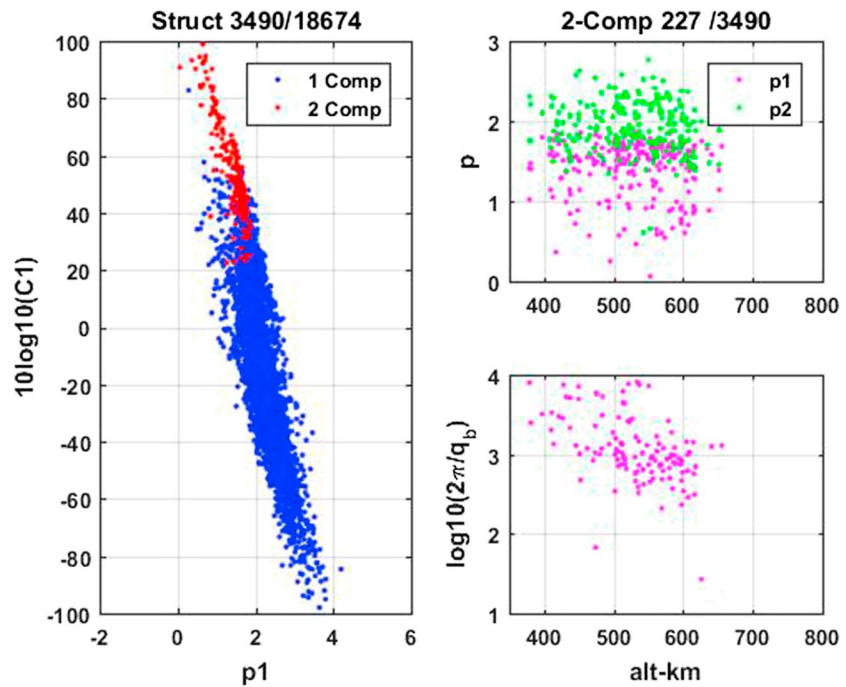


Figure 6. Summary of structured scale spectra for 2014 segments.

The similarity of the patterns from year to year is striking. Each year 19% of the segments are structured. Only 4% to 6% of the structured segments admit two-component power law classification, and these segments are most disturbed. Given the high degree of ESF variability, the classes might be extended or edited. For example, a significant number of the two-component spectra assign negative values to  $p_1$ , which implies increasing spectral intensity with decreasing wave number. An enhancement of the low-frequency spectral components can be interpreted as a transition from intermediate-scale stochastic to

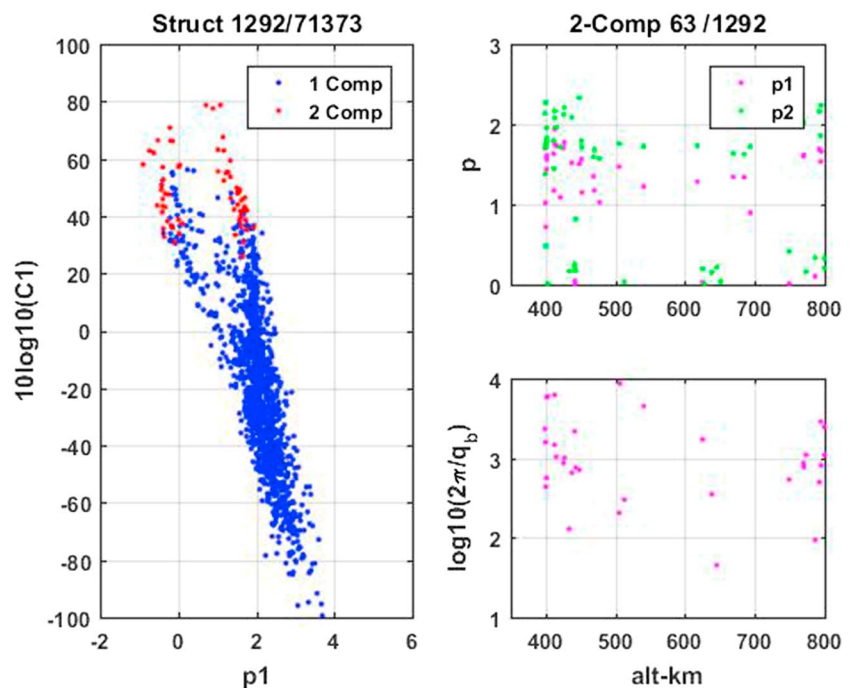


Figure 7. Summary of structured scale spectra for 2011 segments classified with tight threshold used in the original study.

large-scale quasi-deterministic structure. Similarly, the  $C_1$  values approaching  $-100$  dB are associated with steep positive  $p_1$  values, which may indicate an inner scale transition to small-scale structure. For the purposes of this study, intermediate-scale structure characteristics are well established within the scale range from 100 km to 100 m. Note that the only positive  $p_1$  values are plotted in the summary plots to emphasize the main branch of two-component segments.

There is a prominent inverse correlation between  $C_1$  in dB units and  $p_1$ . Two-component segments with positive  $p_1$  values continue the inverse  $C_1$ - $p_1$  correlation. The inverse correlation between  $C_1$  in dB units and  $p_1$  was first observed in in situ rocket measurements [Rino *et al.*, 1981]. While most reported studies of in situ structure were not large enough to confirm the correlation, it has been observed in scintillation data following the early rocket observations [Rino and Liu, 1982], and more recently Wernik *et al.* [2007].

The most probable values of the defining two-component parameters are  $2\pi/q_0 \approx 1000$  m,  $p_1 \approx 1$ , and  $p_2 \approx 2$ . This structure model was in the global ionospheric model PBMOD [Su *et al.*, 2008]. In the cited study by Costa *et al.* [2011] the single power law form with break at 70 m was used. The results of the current study show that the two spectral models apply under different ESF conditions.

A companion paper by Carrano and Rino [2016] addresses the ramifications of two-component power law models for scintillation. Statistical scintillation theory is based on analytic SDF models, which formally extend the constrained range of  $q$  in (1) to  $0 < q < \infty$ . The strong scatter theory of scintillation for a one-dimensional phase screen is based on phase SDFs with the same power law form of as (1). Scintillation theory introduces an additional Fresnel scale parameter

$$\rho_F = \sqrt{r_p/k}, \tag{4}$$

where  $r_p$  is the propagation distance and  $k$  is the electromagnetic wave number. The extended scintillation theory is completely defined by the universal strength parameter

$$U = \begin{cases} U_1 & \mu \leq \mu_0 \\ U_2 & \mu > \mu_0 \end{cases}, \tag{5}$$

where  $\mu = q/\rho_F$ ,  $U_1 = C_p' \rho_F^{p_1-1}$ , and  $U_2 = U_1 \mu_0^{p_2-p_1}$ . The prime is used to distinguish the one-dimensional phase spectral index from the one-dimensional in situ index. The 0 subscript means  $q$  is replaced by  $q_0$ . To connect the measured structure parameters to the extended strong scatter theory,  $C_p'$  must be computed. This requires a three-dimensional structure model, which is summarized in the appendix.

The extended scintillation theory allows a full exploration of the scintillation dependence on the structure parameters. As an example, Figure 8 shows a plot of  $U$  versus the observed span of in situ turbulent strength

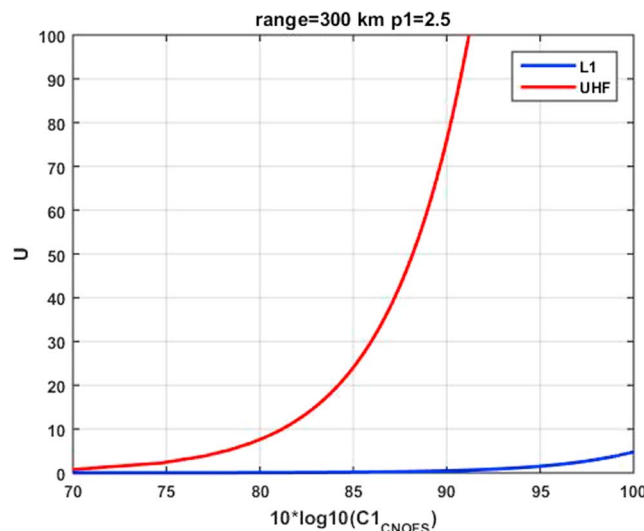


**Figure 8.** Phase screen universal strength for the measured range of unnormalized C/NOFS turbulent strength.

values derived from the C/NOFS measurements reported in the body of this paper distributed over a 50 km path at a distance of 350 km from the source region. When  $U > 1$ , the scintillation index approaches unity. The calculation shows that during any of the 4 years summarized, a significant percentage of ESF structure is strong enough to cause severe fading at the primary GPS frequency (L1 = 1575 MHz).

#### 4. Summary and Discussion

From a detailed analysis of 4 years high-resolution C/NOFS satellite data, we identified intermediate-scale two-component spectra as prominent features in the most highly disturbed

passes. A wavelet-based procedure identified the largest segment length for statistical characterization as 260 km. Between 4% and 6% of the segments were classified as two components. During the 4 year period, solar activity was weak to moderate compared with the previous several solar cycles. The break wave number in the two-component spectra corresponded to 1 km. The large-scale index approached 1. The small-scale index approached 2. The remaining spectra were classified as a single component. The most commonly reported single-component index value is between 1 and 2. We also noted that strong scatter scintillation from VHF to L-Band can be explained by two-component power law structure with parameters in the measured range. We showed further that the structure is qualitatively consistent with GPS observations.

At the present time there is no definitive theoretical support for the results presented in this paper. Physics-based simulations have been used extensively to study the development, evolution, and interaction of large-scale ESF associated with plumes. It is encouraging that the resolution is improving to the point where representative intermediate-scale structure ranges can be generated. The most challenging result to explain is the systematic change in structure with turbulent strength. Possibly the structure evolution is associated with an ESF life cycle. Two-component spectra are observed only in the strongly driven early development phase, possibly with an upward and downward cascade from enhanced convective instability growth at a scale near 1 km. The decay phase is a relaxation to an evolving downward cascade. There are an infinity of structure realizations that have the same SDF. New structure characterizations that accommodate the physical distribution of structure sizes may be needed.

### Appendix A: Structure Models

The interpretation of one-dimensional in situ measurements and remote propagation diagnostics relies on structure models. Following the development in chapters 3 and 4 of *Rino* [2011], we start with the three-dimensional isotropic form:

$$R(\delta r) = C_s \frac{(\delta r / (q_L 2))^{v-1} K_{v-1}(q_L \delta r)}{4\pi^{3/2} \Gamma(v + 1/2)}$$

$$\Phi_{\delta N}(q_3) = C_s (q_L^2 + q_3^2)^{-(v+1/2)}. \tag{A1}$$

To accommodate magnetic-field-aligned anisotropy, a transformation from a field-aligned and stretched coordinate system is used:

$$\delta r = \zeta_{\text{eff}} \delta \eta \tag{A2}$$

$$\zeta_{\text{eff}} = \sqrt{\mathbf{u}^T U^T D U \mathbf{u}}. \tag{A3}$$

The diagonal matrix  $D$  defines elongation factors along and transverse to the principal elongation axis. The matrix  $U$ , not to be confused with the universal strength parameter, rotates the scaled principal axis coordinates onto the reference system.

The observable one-dimensional in situ SDF is defined by the cosine transformation of  $R_{\delta N}(\zeta_{\text{eff}} \delta \eta)$ :

$$\varphi(q) = 2 \int_0^\infty R_{\delta N}(\zeta_{\text{eff}} \delta \eta) \cos(q \delta \eta) d\delta \eta. \tag{A4}$$

The integral can be evaluated analytically:

$$\varphi(q) = C_s \frac{\zeta_{\text{eff}}^{2v-2}}{2\pi(2v-1)} \left( (\zeta_{\text{eff}} q_L)^2 + q^2 \right)^{-v+1/2}. \tag{A5}$$

For  $q \gg q_L \zeta_{\text{eff}}$ ,

$$\varphi(q) \simeq \left[ C_s \frac{\zeta_{\text{eff}}^{2v-2}}{2\pi(2v-1)} \right] q^{-(2v-1)}. \tag{A6}$$

Thus,  $C_s$  can be computed from measured one-dimensional parameters  $C_1$ ,  $\nu = (p_1 + 1)/2$ , and the geometric factor  $\zeta_{\text{eff}}$ :

$$C_s = 2\pi(2\nu - 1)\zeta_{\text{eff}}^{-(2\nu-2)}C_1. \quad (\text{A7})$$

To maintain consistent units, scale spectra have been normalized to coincide with the unweighted periodogram. The scale spectra intensities,  $SCD_n$ , satisfy the relation

$$\frac{1}{N_s} \sum_{k=0}^{N_s-1} |N_k|^2 = \frac{1}{N_s} \sum_{n=0}^{N_s-1} SCD_n. \quad (\text{A8})$$

To be consistent with the functional SDF  $\varphi(k\Delta q)$ ,

$$\frac{1}{N_s} \sum_{k=0}^{N_s-1} |\hat{N}_k|^2 = \sum_{k=0}^{N_s-1} |\varphi(k\Delta q)|^2 \frac{\Delta q}{2\pi}. \quad (\text{A9})$$

With a final scale factor to convert the C/NOFS cgs units to mks,

$$CF = \Delta q / (2\pi N_s) 10^{12} = \Delta s 10^{12}, \quad (\text{A10})$$

converts measured scale spectra to mks units.

From the statistical theory of scintillation the two-dimensional phase from integration along the propagation path is characterized by

$$R_{\delta\phi}(y_2) = \frac{C_p^{(2)} (q_L/2)^{-\nu+1/2}}{2\pi\Gamma(\nu+1/2)} y^{\nu-1/2} K_{\nu-1/2}(q_L y_2) \quad (\text{A11})$$

$$\Phi_{\delta\phi}(q_2) = C_p^{(2)} (q_L^2 + q_2^2)^{-(\nu+1/2)} \quad (\text{A12})$$

where

$$C_p^{(2)} = 4\pi^2 r_e^2 l_p \sec \theta GC_s / k^2 \quad (\text{A13})$$

$r_e = 2.819740289e-15$  m,  $k = 2\pi f_c / c$ ,  $l_p$  is the path length, and

$$G = \frac{ab \sec \theta}{\sqrt{AC - B^2/4}}. \quad (\text{A14})$$

The propagation direction is defined by the angle  $\theta$  from vertical and an azimuth angle  $\phi$ . The parameters  $a$  and  $b$  are structure elongation factors. The geometric factors  $A$ ,  $B$ , and  $C$  are functions of the propagation angles. All the parameters and geometric translations are summarized in Appendix A.3 of *Rino and Liu* [1982].

The one-dimensional phase autocorrelation that characterizes the phase screen is

$$R_{\delta\phi}(\xi_{\text{eff}}\mathcal{Y}) = \frac{C_p^{(2)}}{\pi\Gamma(\nu+1/2)} (\xi_{\text{eff}}\mathcal{Y} / (2q_L))^{\nu-1/2} K_{\nu-1/2}(q_L \xi_{\text{eff}}\mathcal{Y})$$

$$\varphi_{\delta\phi}(q) = C_p^{(1)} \left( (q_L \xi_{\text{eff}})^2 + q^2 \right)^{-\nu}, \quad (\text{A15})$$

where

$$C_p^{(1)} = \frac{C_p^{(2)}\Gamma(\nu)}{2\sqrt{\pi}\Gamma(\nu+1/2)} \xi_{\text{eff}}^{2\nu-1}, \quad (\text{A16})$$

and

$$\xi_{\text{eff}} = \frac{Cu_{ky}^2 - Bu_{ky}u_{kz} + Au_{kz}^2}{AC - B^2/4}, \quad (\text{A17})$$

where  $u_{kx}$ ,  $u_{ky}$ , and  $u_{kz}$  define a unit vector along the propagation direction. The one-dimensional phase spectral index is  $p' = 2\nu = p_1 - 1$ .

Equations (A7) and (A10) convert measured  $C_1$  and  $p_1$  to the corresponding three-dimensional model parameters. Equation (A16) converts the three-dimensional model parameters to the corresponding one-dimensional phase screen parameters. The model calculations are for single power law spectra, but the error in applying them to the large-scale component of a two-component structure should not be prohibitively large.

#### Acknowledgments

The data used for this study were made available for the study by the Air Force Research Laboratory. The MATLAB analysis procedures can be downloaded from MatLab Central File Exchange <http://www.mathworks.com/matlabcentral/fileexchange/35092-wavelet-scale-spectra>.

#### References

- Aveiro, H. C., D. L. Hysell, R. G. Caton, K. M. Groves, J. Klenzing, R. F. Pfaff, R. Stoneback, and R. A. Heelis (2012), Three-dimensional numerical simulations of equatorial spread  $F$ : Results and observations in the Pacific sector, *J. Geophys. Res.*, *117*, A03325, doi:10.1029/2011JA017077.
- Carrano, C. S., and C. L. Rino (2016), A theory of scintillation for two-component power law irregularity spectra: 1. Overview and numerical results, *Radio Sci.*, *51*, RS2011, doi:10.1002/2015RS005903.
- Costa, E., E. R. de Paula, L. F. C. Rezende, K. M. Groves, P. A. Roddy, E. V. Dao, and M. C. Kelley (2011), Equatorial scintillation calculations based on coherent scatter radar and C/NOFS data, *Radio Sci.*, *46*, RS2011, doi:10.1029/2010RS004435.
- Costa, E., P. A. Roddy, and J. O. Ballenthin (2014), Statistical analysis of C/NOFS Planar Langmuir Probe data, *Ann. Geophys.*, *32*, 77–791, doi:10.5194/angeo-32-773-2014.
- Dao, E., M. C. Kelley, D. L. Hysell, J. M. Retterer, Y. J. Su, R. F. Pfaff, P. A. Roddy, and J. O. Ballenthin (2012), On the distribution of ion density depletion along magnetic field lines as deduced using C/NOFS, *Radio Sci.*, *47*, RS3001, doi:10.1029/2011RS004967.
- de La Beaujardiere, O. (2003), Communication/navigation outage forecasting system (C/NOFS) science plan, *Tech. Rep. AFRL/VS-TR-2003-1501*, Air Force Res. Lab., Kirkland AFB.
- Franke, S. J., C. H. Liu, and D. J. Fang (1984), Multifrequency study of ionospheric scintillation at Ascension Island, *Radio Sci.*, *19*(3), 695–706.
- Huang, C.-S., O. de la Beaujardière, P. A. Roddy, D. E. Hunton, R. F. Pfaff, C. E. Valladares, and J. O. Ballenthin (2011), Evolution of equatorial ionospheric plasma bubbles and formation of broad plasma depletions measured by the C/NOFS satellite during deep solar minimum, *J. Geophys. Res.*, *116*, A03309, doi:10.1029/2010JA015982.
- Huang, C.-S., O. de la Beaujardière, P. A. Roddy, D. E. Hunton, J. O. Ballenthin, M. R. Hairston, and R. F. Pfaff (2013), Large-scale quasiperiodic plasma bubbles: C/NOFS observations and causal mechanism, *J. Geophys. Res. Space Physics*, *118*, 3602–3612, doi:10.1002/jgra.50338.
- Huang, C.-S., O. de la Beaujardière, P. A. Roddy, D. E. Hunton, J. Y. Liu, and S. P. Chen (2014), Occurrence probability and amplitude of equatorial ionospheric irregularities associated with plasma bubbles during low and moderate solar activities (2008–2012), *J. Geophys. Res. Space Physics*, *119*, 1186–1199, doi:10.1002/2013JA019212.
- Hysell, D. L. (2000), An overview and synthesis of plasma irregularities in equatorial spread  $F$ , *J. Atmos. Terres. Phys.*, *62*, 1037–1056.
- Klenzing, J. H., D. E. Rowland, R. F. Pfaff, G. Le, H. Freudenreich, R. A. Haaser, A. G. Burrell, R. A. Stoneback, W. R. Coley, and R. A. Heelis (2011), Observations of low-latitude plasma density enhancements and their associated plasma drifts, *J. Geophys. Res.*, *116*, A09324, doi:10.1029/2011JA016711.
- Nishioka, M., S. Basu, S. Basu, C. E. Valladares, R. E. Sheehan, P. A. Roddy, and K. M. Groves (2008), C/NOFS satellite observations of equatorial ionospheric plasma structures supported by multiple ground-based diagnostics in October 2008, *J. Geophys. Res.*, *116*, A10323, doi:10.1029/2011JA016446.
- Retterer, J. M., and P. Roddy (2014), Faith in a seed: On the origins of equatorial plasma bubbles, *Ann. Geophys.*, *32*, 485–498, doi:10.5194/angeo-32-485-2014.
- Rino, C. L. (2011), *The Theory of Scintillation With Applications in Remote Sensing*, John Wiley, New York.
- Rino, C. L., and C. H. Liu (1982), Intensity scintillation parameters for characterizing transionospheric radio signals, *Radio Sci.*, *17*(1), 279–284.
- Rino, C. L., R. T. Tsunoda, J. Petriceks, R. C. Livingston, M. C. Kelley, and K. D. Baker (1981), Simultaneous rocket-borne beacon and in situ measurements of equatorial spread  $F$ : Intermediate wavelength results, *J. Geophys. Res.*, *86*(A4), 2411–2419.
- Rino, C. L., C. S. Carrano, and P. A. Roddy (2014), Wavelet-based analysis and power law classification of C/NOFS high-resolution electron density data, *Radio Sci.*, *49*, 680–688, doi:10.1002/2013RS005272.
- Roddy, P. A., D. E. Hunton, O. Ballenthin, and K. M. Groves (2010), Correlation of in situ measurements of plasma irregularities with ground-based scintillation observations, *J. Geophys. Res.*, *115*, A06303, doi:10.1029/2010JA015288.
- Rodrigues, F. S., M. C. Kelley, P. A. Roddy, D. E. Hunton, R. F. Pfaff, O. de la Beaujardière, and G. S. Bust (2009), C/NOFS observations of intermediate and transitional scale-size equatorial spread  $F$  irregularities, *Geophys. Res. Lett.*, *36*, L00C05, doi:10.1029/2009GL038905.
- Stoneback, R. A., R. A. Heelis, R. G. Caton, Y. J. Su, and K. M. Groves (2013), In situ irregularity identification and scintillation estimation using wavelets and CINDI on C/NOFS, *Radio Sci.*, *48*, 388–395, doi:10.1002/rds.20050.
- Su, Y.-J., J. M. Retterer, O. de La Beaujardière, W. J. Burke, P. A. Roddy, R. F. Pfaff Jr., G. R. Wilson, and D. E. Hunton (2008), Assimilative modeling of equatorial plasma depletions observed by C/NOFS, *Geophys. Res. Lett.*, *36*, L00C02, doi:10.1029/2009GL038946.
- Wernik, A. W., L. Alfonsi, and M. Materassi (2007), Scintillation modeling using in situ data, *Radio Sci.*, *42*, RS1002, doi:10.1029/2006RS003512.